Unravelling the Chemical and Structural Evolution of Mn and Ti in Disordered Rocksalt Oxyfluoride Cathode Materials Using *Operando* X-ray Absorption Spectroscopy

Yasaman Shirazi Moghadam, Yang Hu,* Abdel El Kharbachi, Stéphanie Belin, Thomas Diemant, Jun Chen, Robert A. House, Peter G. Bruce, and Maximilian Fichtner

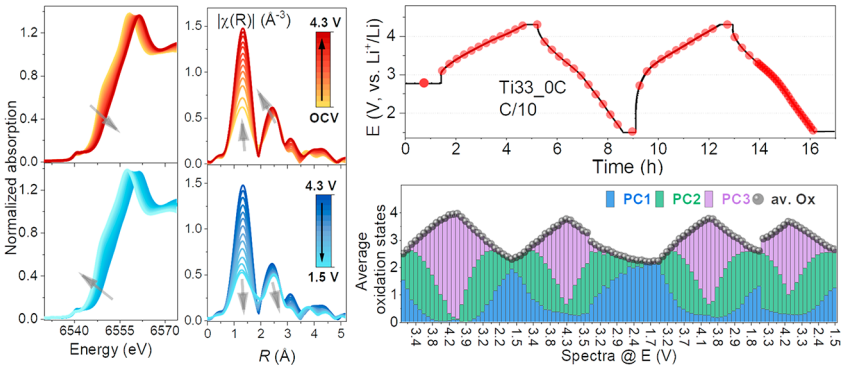

ABSTRACT: Li-rich disordered rocksalt (DRS) cathode materials with naturally abundant resources, high power and energy density have attracted great attention for applications in Li-ion batteries. We have previously investigated the $Li_2Mn_{1-x}Ti_xO_2F$ ($0 \leq x \leq 2/3$, LMTOF) cathode system showing an attractive cycling behavior, which is however limited by poor long-cycle stability and the unclear cation and anion redox activities in the presence of supposedly inactive Ti. In this work, synchrotron *operando* X-ray absorption spectroscopy (XAS) is performed to study the chemical and structural evolution of Mn and Ti in the cathode compounds during cycling. Selected electrodes with low (x = 1/3) and high (x = 2/3) Ti content are synthesized, and their structural and electrochemical properties are first characterized accordingly. X-ray absorption near-edge structure (XANES) and extended X-ray absorption fine structure (EXAFS) are combined to track the change in oxidation states and local coordination environment for the active transition metals. In order to follow the dynamics of the active species, chemometric methods such as principal component analysis (PCA) and multivariate curve resolution (MCR) are applied. Subsequently, the Mn and Ti redox activities are monitored from initial to extended cycles, in combination with *ex-situ* studies and *operando* differential electrochemical mass spectrometry (DEMS) to understand the capacity fading and the redox-based degradation processes. The results provide insights into the development of Mn double-redox reactions in the DRS cathodes from initial cycles to prolonged cycling and elucidate the impacts of the reduced Mn redox activity and the increased local ordering on the cycling stability.

1. INTRODUCTION

With the looming energy crisis and environmental pollution, Li-ion batteries as the most promising candidates to store green energy resources have attracted significant attention in the last decades. Meanwhile, this application has rapidly expanded from portable electronic devices to large-scale smart grids and electric vehicles.[1,2] In constant pursuit of advanced cathode materials for higher energy storage and better performance, a lot of effort has been dedicated to the development of material systems with low-cost, eco-friendly, and naturally abundant resources in order to reduce the dependence on rare transition metals limited by geopolitical restrictions such as nickel and cobalt.[2−4]

Recently, vast research progress has been made in the field of Li-rich disordered rocksalt (DRS) materials aiming to exploit high power and energy density batteries with environment-friendly and nature-abundant metals, such as Mn, Ti, and others.[5−8] Manganese is an attractive redox-active transition metal for Li-rich DRS materials, as it allows

multielectron transfer. In addition, manganese is an inexpensive and earth-abundant element which is economically desirable for manufacturing high-energy Li-ion batteries.[9,10] Compositions within the formula range $Li_2Mn_{1-x}Ti_xO_2F$ ($0 \leq x \leq 2/3$)—LMTOF, which combine the high-valent cations substitution and the partial substitution of F^- for O^{2-} anions,[1] have been proposed as cobalt-free high-energy cathode materials for Li-ion batteries. The high-valent Ti^{4+} as a $3d^0$ transition metal (TM) promotes the formation of a disordered rocksalt structure. Also, the low-valent F^- sets up the charge balance to favor the incorporation of Mn as Mn^{2+} in the structure, allowing the Mn^{4+}/Mn^{2+} double-redox reaction. Particularly, previous studies showed that the composition $Li_2Mn_{2/3}Ti_{1/3}O_2F$ (Ti33) with Ti^{4+} and mixed $Mn^{2+/3+}$ in the initial state demonstrated better cycling stability.[11−13] After the initial charge, this composition can deliver a discharge capacity comparable to the Li-rich layered NMC (200−220 mAh/g)[14,15] and greater than the conventional LCO (170 mAh/g).[16] Furthermore, a capacity retention of 190 mAh/g (~650 Wh/kg) after 100 cycles and 136 mAh/g (~460 Wh/kg) after 200 cycles was obtained.[11] All of the aforementioned performance features make the LMTOF system appealing as a candidate for cobalt-free cathode materials. To further improve the capacity retention of this LMTOF system, the current understanding of the structural evolution and its redox chemistry needs to be improved, especially for the reaction mechanisms and degradation phenomena during long-time cycling. For instance, the change of Mn redox due to oxygen loss at high voltage, along with the Mn dissolution inside the electrolyte, are known to be responsible for the capacity fading of Li-rich Mn based cathode materials.[17−19] Moreover, Ti cations are commonly considered to be inactive during cycling,[20] but the real evolution of Ti in a disordered system and their change in oxidation state after prolonged cycling have not been elucidated yet.

X-ray absorption spectroscopy (XAS) has been well established as a powerful tool to probe the battery chemistry and materials functionality; especially under *operando* conditions, the real-time chemical and electronic information can be achieved.[3,4] In this work, *operando* XAS with a synchrotron source is applied to understand the redox chemistry and the cycling-induced local structure evolution in Li-rich DRS LMTOF cathode materials, aiming to identify the limiting factors of the cycling stability and to eventually accelerate their further development as cobalt-free high-energy cathode materials for Li-ion batteries.

2. EXPERIMENTAL SECTION

2.1. Synthesis. The $Li_2Mn_{1-x}Ti_xO_2F$ (x = 0, 1/3, 1/2, and 2/3, referred as Ti0, Ti33, Ti50, and Ti66) powder materials, were synthesized in two steps using high energy mechanochemical ball-milling processes as described elsewhere.[11] Li_2O (99.7%), Mn_2O_3 (99%), Ti_2O_3 (99.8%), and LiF (99.9%) (all from Alfa Aesar) were mixed in stoichiometric ratios under an inert atmosphere using silicon nitride jar (80 mL) and balls (10 mm) as grinding media, with a constant ball-to-powder weight ratio of 25:1. After milling, the powders were recovered from the jar in an Ar-filled glovebox and sieved using a 200 mesh sieve (USA standard sieve series). In this work, $Li_2Mn_{2/3}Ti_{1/3}O_2F$ (Ti33) and $Li_2Mn_{1/3}Ti_{2/3}O_2F$ (Ti66) were selected as the main subjects of interest. In addition, Li_2MnO_2F (Ti0) and laboratory-synthesized DRS $LiMnO_2$ were used as reference standards owing to the same disordered rocksalt structure.

2.2. Materials Characterization. The final phase of the synthesized materials was verified by powder X-ray diffraction using a STOE STADI-P diffractometer in transmission geometry (Mo $K\alpha_1$ radiation, λ = 0.70932 Å). Powder samples were sandwiched between two acetate foils and sealed inside an airtight XRD sample holder.

Transmission electron microscopy (TEM) measurements were carried out on a Themis300 electron microscope working at 300 kV and equipped with a DCOR probe corrector and a Super X EDX detector. The dry powders were directly dispersed on a TEM holey carbon membrane without using solvents. All samples were prepared in an Ar-filled glovebox and transferred to the microscope using an airtight vacuum transfer holder. The *K*-lines of O, F, Ti, and Mn were used for quantification in scanning transmission electron microscopy (STEM)-EDX.

The chemical state of the Mn in the topmost surface layer (sampling depth ~3−5 nm) for Li_2MnO_2F and $LiMnO_2$ was analyzed by X-ray photoelectron spectroscopy (XPS) with a PHI 5800 Multi-Technique ESCA System (Physical Electronics). To avoid surface contamination, the samples were prepared in an Ar-filled glovebox and transferred to the XPS system using a sealed vessel. The measurements were carried out using monochromatized Al Kα radiation (250 W, 15 kV), a detection angle of 45°, and analyzer pass energies of 93.9 and 29.35 eV for survey and detail spectra, respectively. The samples were neutralized with electrons from a flood gun (current *ca.* 3 μA). For binding energy calibration, the C 1*s* main peak was set to 284.8 eV. Peak fitting was accomplished by using the CasaXPS program package with a Shirley-type background and Gaussian−Lorentzian peak profiles.

2.3. Electrodes and Cells Preparation. To enhance the electronic conductivity, 70 mg of the active compounds and 20 mg of super P carbon black were first premixed for 3 h under an inert atmosphere using 20 mL silicon nitride (SN) vial with 10 SN balls (Ø 2 mm) as grinding agents in a P7 planetary ball mill. Composite electrodes were prepared with 70 wt % active materials, 20 wt % super P carbon black, and 10 wt % poly(vinylidene fluoride) (PVDF) binder dissolved in *N*-methyl-2-pyrrolidone (NMP) using a Thinky mixer (ARE-250, Thinky Inc.). The obtained slurry was coated on aluminum foil using an automatic doctor blade machine inside an Ar-filled glovebox. The coating was then dried overnight at 120 °C in a vacuum oven and a 12 mm disk of the electrode was punched to be used as positive electrode. The typical loading of the active material on the aluminum foil disk was fixed at 2.5 ± 0.2 mg cm^{-2}. In addition, high-loading-mass electrodes (3−4 mg cm^{-2}) were selected for *operando* XAS measurements to increase the signal-to-noise ratio.

The laboratory electrochemical characterizations were carried out with two-electrode Swagelok-type cells, in which 1 M $LiPF_6$ in ethylene carbonate/diethyl carbonate (EC/DEC) solvent mixture (1:1, BASF), Whatman glass fiber, and Li-metal foil were used as electrolyte, separator, and counter/reference electrode, respectively. The cells were assembled in an Ar-filled glovebox and kept there for 24 h prior to the electrochemical tests.

2.4. Electrochemical Characterizations. Cyclic voltammetry (CV) was performed on selected Ti33 and Ti66 samples using a VMP-3 Potentiostat from Bio-Logic over the potential range 1.5−4.3 V and at various scan rates (0.1, 0.5, 5, and 10 mV/s).

To prepare the precycled electrodes for synchrotron XAS, the cells were cycled at 25 °C in the voltage range from 1.5 to 4.3 V at two C-rates (1C and 0.1C, based on theoretical capacity for 2 Li per formula unit) and up to various cycle numbers (1, 9, 10, 49, 50, 99, 100, and 200 cycles) using an Arbin BT2000 electrochemical cycler. After cycling, the cells were disassembled in an Ar-filled glovebox and the positive electrodes were collected and washed three times with DMC to be free from additional salts and solvents. The electrodes were then dried overnight in a vacuum oven inside the glovebox and then sealed for transport.

Operando differential electrochemical mass spectrometry (DEMS) analysis was carried out to determine the presence and composition of different gases evolved during galvanostatic cycling. A working electrode (70 wt % active materials, 20 wt % Super P carbon black, and 10 wt % polytetrafluoroethylene (PTFE) binder), two Whatman glass fiber separators containing the electrolyte (1 M $LiPF_6$ in propylene carbonate), and a lithium metal counter electrode were

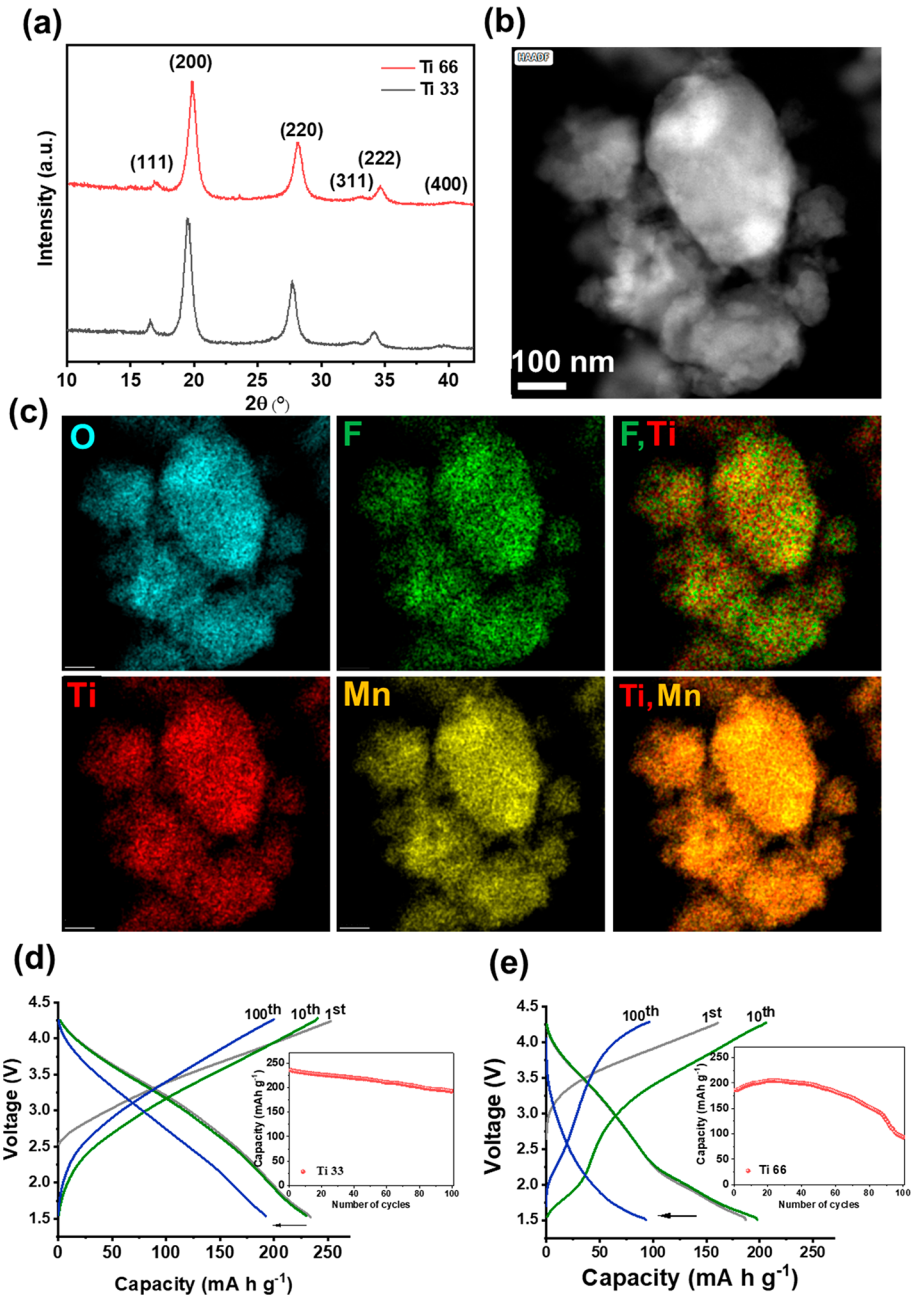

Figure 1. (a) X-ray diffraction patterns of as-synthesized Ti33 and Ti66 samples, attributed to a cubic rocksalt phase (space group $Fm\bar{3}m$). (b) HAADF STEM image with (c) the corresponding EDX mapping for the Ti33 sample. Galvanostatic cycling profiles and cyclability plots of (d) Ti33 and (e) Ti66 electrodes (1.5–4.3 V, 0.1 C, 25 °C).

assembled into a two-electrode type cell (ECC-Std from EL-CELL) with gas inlet and outlet inside an Ar-filled glovebox. The cell was further connected to a quadrupole mass spectrometer (Thermo Fisher) equipped with a turbomolecular pump (Pfeiffer Vacuum) and mass-flow controllers (Bronkhorst). During the *operando* DEMS measurements, high-purity Ar gas at a rate of 1 mL/min was used as the carrier gas, and the cell was charged/discharged with a constant current (10 mA/g) in a voltage window of 1.5–4.8 V at room temperature using a Biologic VMP3 potentiostat.

2.5. Synchrotron XAS. Mn and Ti *K*-edge XAS measurements were carried out in transmission mode on the ROCK beamline at the SOLEIL Synchrotron facility (Proposal number 20210779).[21,22] Two Si(111) quickexafs monochromators were used with an oscillation speed of 2 Hz at the Mn and the Ti *K*-edge enabling the collection of one full absorption spectrum in 250 ms. The signal was collected in transmission using three gas ionization chambers as detectors, which in series allowed the simultaneous recording of the incident beam, the beam transmitted by the sample, and the beam transmitted by a sheet of Mn/Ti metal foil; the latter was used as a reference for energy calibration.

A Swagelok-type *in-situ* cell with two Be windows was used for *operando* measurements.[23] The working electrode, the separator (soaked with electrolyte), and the lithium counter electrode (all the same as those used in laboratory Swagelok cells) were stacked layer by layer between a large Be window and a stainless steel plunger with a smaller Be window. All cell preparation was done inside an Ar-filled glovebox. Reference standards were prepared by diluting MnO, Mn_2O_3, MnO_2, Ti_2O_3, and TiO_2 powders with cellulose and pressing them into pellets; as-synthesized pristine $Li_2Ti_xMn_{1-x}O_2F$ (x = 0, 1/3, 1/2, 3/2) and DRS $LiMnO_2$ samples were also prepared in the same way.

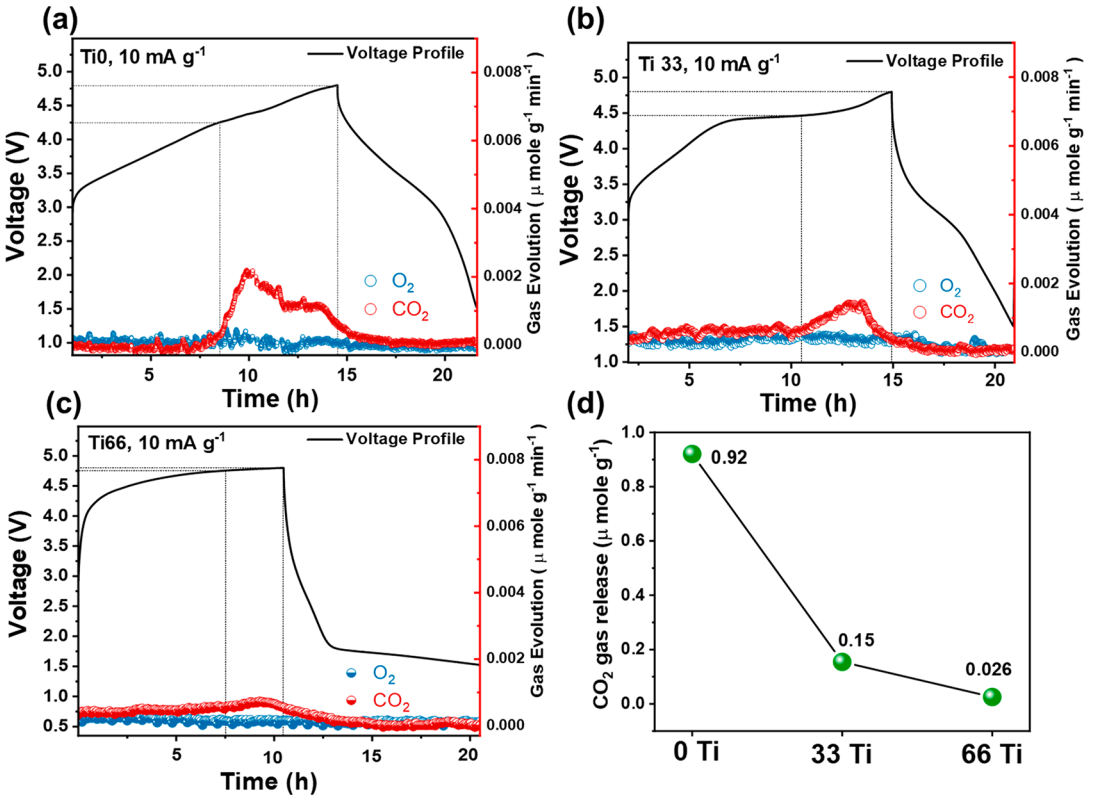

Figure 2. *Operando* DEMS results from half cells with (a) Ti0-, (b) Ti33-, and (c) Ti66-based electrodes during the first cycle. The solid lines, blue circles, and red dots correspond to the voltage profiles, O_2 evolution, and CO_2 evolution, respectively; (d) the total amount of released CO_2 calculated based on the area under the CO_2 evolution curve for each sample. The gas evolution is given in μmol of gas species released per gram of active material.

During the *operando* XAS measurements, the electrochemical cells were galvanostatically cycled under ambient conditions within the voltage window of 1.5−4.3 V at a cycling rate of 0.1 C (based on the theoretical capacity of the electrode) with a BioLogic VMP3 battery cycler. Mn *K*-edge absorption spectra were extracted and averaged over 590 scans (elapsed time, 292 s; exposure, 146 s). The cycling profiles with the points of XAS data acquisition are shown in Figures S1a−c. For the Ti66 sample with higher Ti content, Mn and Ti *K*-edge XAS were alternatively measured, as shown in Figure S1d. The energy grids of extracted spectra are listed in Table S1. In addition, other precycled electrode tapes were sealed in polyethylene bags inside an Ar-filled glovebox. They were taken out of the glovebox shortly before being measured *ex-situ*, together with the reference standards and pristine materials.

XAS data were further analyzed with Fastosh,[24] Athena of Demeter packages[25] and Larch[26] software. The calibrated and normalized XANES spectra were compared with reference standards to fingerprint the oxidation states and the electronic structure. Principle components analysis (PCA) and multivariate curve resolution by alternating least-squares (MCR-ALS) were performed on normalized spectra from the *operando* measurements of fresh Ti33 and Ti66 electrodes to extract the possible intermediate constituents and their evolution during cycling. Linear combination fits (LCF) were also carried out on normalized Mn spectra over the range from 6520 to 6625 eV based on experimental spectra of selected standards. In addition, the concentration profiles of precycled Ti33_49C and Ti33_99C electrodes were obtained by LCF using the theoretical component spectra obtained from the MCR-ALS of fresh Ti33_0C electrode. EXAFS spectra were extracted using the AUTOBK algorithm[27] and further Fourier transformed (FT) after applying a Hanning window function over an appropriate data range (Table S2). In order to probe the local structure and coordination environment for Mn and Ti, shell fitting was performed using theoretical models computed by FEFF8 in Larch.[26,28] More details are described in the Supporting Information.

3. RESULTS AND DISCUSSION

3.1. Materials Characterization. Li-rich DRS $Li_2Mn_{0.66}Ti_{0.33}O_2F$ (Ti33) and $Li_2Mn_{0.33}Ti_{0.66}O_2F$ (Ti66) were synthesized using mechanochemical synthesis and the disordered rocksalt structure was successfully formed as nanocrystals (Figure 1a). A shift of XRD reflection peaks toward higher 2θ angles was observed for Ti66, indicating a slight decrease in lattice parameter.[11] Figure 1b,c displays a high-angle annular dark-field (HAADF) STEM image, combined with the results of EDX mapping for the Ti33 sample. Small primary particles together with nanosized aggregates were observed, and the different shapes and orientations were typical for polycrystalline particles. The EDX results demonstrated a homogeneous distribution of all elements within the sample. Figure 1d,e shows the galvanostatic cycling plots of the two electrodes measured in half cells up to 100 cycles. The Ti33 with a higher amount of Mn, which is the main redox element that undergoes an electrochemical double redox process upon cycling, showed higher initial capacities as well as better capacity retention upon cycling. In contrast to the steady sloping profile of Ti33, Ti66 showed a plateau-like feature below 2.0 V, suggesting a possible redox reaction at low voltage. To gain more insight into the redox reactions happening during the cycling of the samples, cyclic voltammetry with different scan rates (0.1, 0.5, 5, and 10 mV/s) was measured (Figure S2). The Ti33 sample showed two consecutive redox processes approximately at

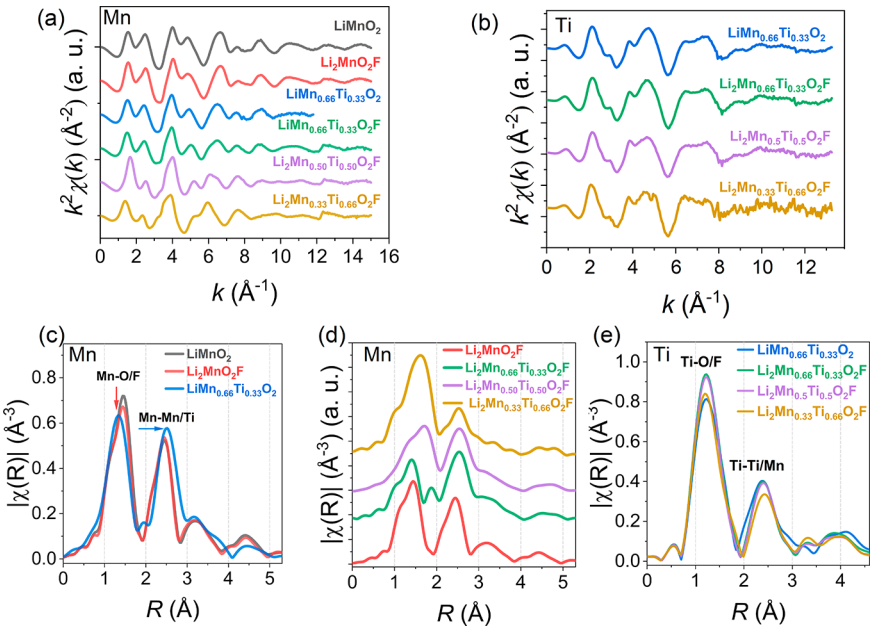

Figure 3. EXAFS spectra of pristine materials measured *ex-situ* at Mn and Ti *K*-edges: k^2-weighted $\chi(k)$ spectra and their corresponding magnitude of Fourier transform for (a, c, d) Mn and (b, e) Ti. $LiMn_{0.66}Ti_{0.33}O_2$ was measured on as-prepared electrode tape; all other samples were diluted pellets.

around 3 and 3.5 V. On the other hand, in agreement with the low-voltage plateau in the galvanostatic cycling profile, the Ti66 sample demonstrated additional redox peaks in the low voltage region, which were clarified using further measurement techniques.

Figure 2 presents the results of real-time gas evolution of Ti0, Ti33, and Ti66 electrodes in a two-electrode half-cell during the first cycle, obtained from *operando* differential electrochemical mass spectrometry (DEMS). O_2 and CO_2 were measured while charging the cells from open-circuit voltage (OCV) to 4.8 V followed by discharge to 1.5 V, all at a rate of 10 mA g^{-1}. The results showed no evidence of direct evolution of the O_2 in all of the samples. However, a small amount of CO_2 was evolved in the range of 4.3 V−4.8 V (vs Li^+/Li) at the end of the first charge. The CO_2 most likely originated from reactions between reactive oxidized O species at the cathode surface and the carbonate-based electrolytes.[20,29−36] The total amounts of CO_2 detected from each material (<1 μmol/g) corresponded to less than 1 mAh/g of charging capacity, so the overall extent of oxygen loss from these materials was very small. With an increase in Ti substitution from 0 to 66%, the quantity of detected CO_2 was reduced. For the Ti0 sample, two CO_2 peaks could be discerned and the first one (starting at 4.25 V) had more contributions from the lost lattice O that reacted with electrolyte and the surface Li_2CO_3 species.[36] For the Ti66 sample, CO_2 was only produced beyond 4.75 V where the electrolyte oxidation happened,[36] indicating that the Ti substitution helped to stabilize the cathode materials by suppressing the lattice oxygen loss.

In the next step, XAS measurements were carried out on the as-synthesized pristine LMTOF samples with varying Ti and F content. Figure S4 shows the normalized Mn and Ti *K*-edge XANES spectra of the LMTOF, together with the reference standards. In agreement with our previous works measured with a laboratory instrument,[11] a shift of the Mn *K*-edge toward lower energy was noted with increasing Ti content for the $Li_2Mn_{1-x}Ti_xO_2F$ ($0 \le x \le 2/3$) samples, reflecting a gradual decrease of the Mn oxidation state by introducing higher-valent Ti, from *ca.* 3+ in $LiMnO_2$ (LMO) and Li_2MnO_2F (LMOF, Ti0) to close to 2+ in $Li_2Mn_{0.33}Ti_{0.66}O_2F$ (Ti66). For the Ti *K*-edge, only the Ti66 sample showed a slight edge shift toward lower energy, while all other compounds exhibited the same edge energy, evidencing a reduced Ti oxidation state in Ti66. In addition to oxidation states, EXAFS results demonstrated the change of the Mn and Ti local coordination environment upon cation and anion substitution (Figure 3). The Fourier transform (FT) of weighted $\chi(k)$ represents the radial distribution of half-path lengths (R)—the interatomic distance between the central absorbers (Mn or Ti) and the neighboring scattering atoms. The global $\chi(k)$ is a summation of all scattering paths in the material, in which the faster/slower component oscillations correspond to the longer/shorter path lengths ($2R$) and can be represented as peaks located at respective R (R with a constant phase shift for all contributions) in the plot of magnitude of FT ($|\chi(R)|$); the amplitude of $\chi(k)$ oscillations determines the amplitude of the $|\chi(R)|$ peaks.[37] For Mn, Li_2MnO_2F showed a slight decrease of amplitude in the first coordination shell (Mn−O/F) compared to the parent compound $LiMnO_2$, while a 6-fold TM−ligand octahedral coordination was preserved (Figure 3c). This presumably resulted from the increased local disordering by F substitution for O. When 33% Ti was substituted for Mn in $LiMn_{0.66}Ti_{0.33}O_2$ (LMTO), the first shell Mn−O bond length slightly shortened while R for the second Mn−Mn/Ti shells increased. In the case of $Li_2Mn_{1-x}Ti_xO_2F$ with a constant fluorination and increasing Ti content x from 0 to 2/3 (Figure 3d), stronger modulation and disordering were introduced, leading to a general increase of average interatomic distance for both the first and the second coordination shells. Compared to Mn, the change in the local environment of Ti was modest (Figure 3e) with slight variations of $R_{Ti-O/F}$ and $R_{Ti-Ti/Mn}$. Only the Ti66 sample demonstrated a pronounced increase in $R_{Ti-Ti/Mn}$.

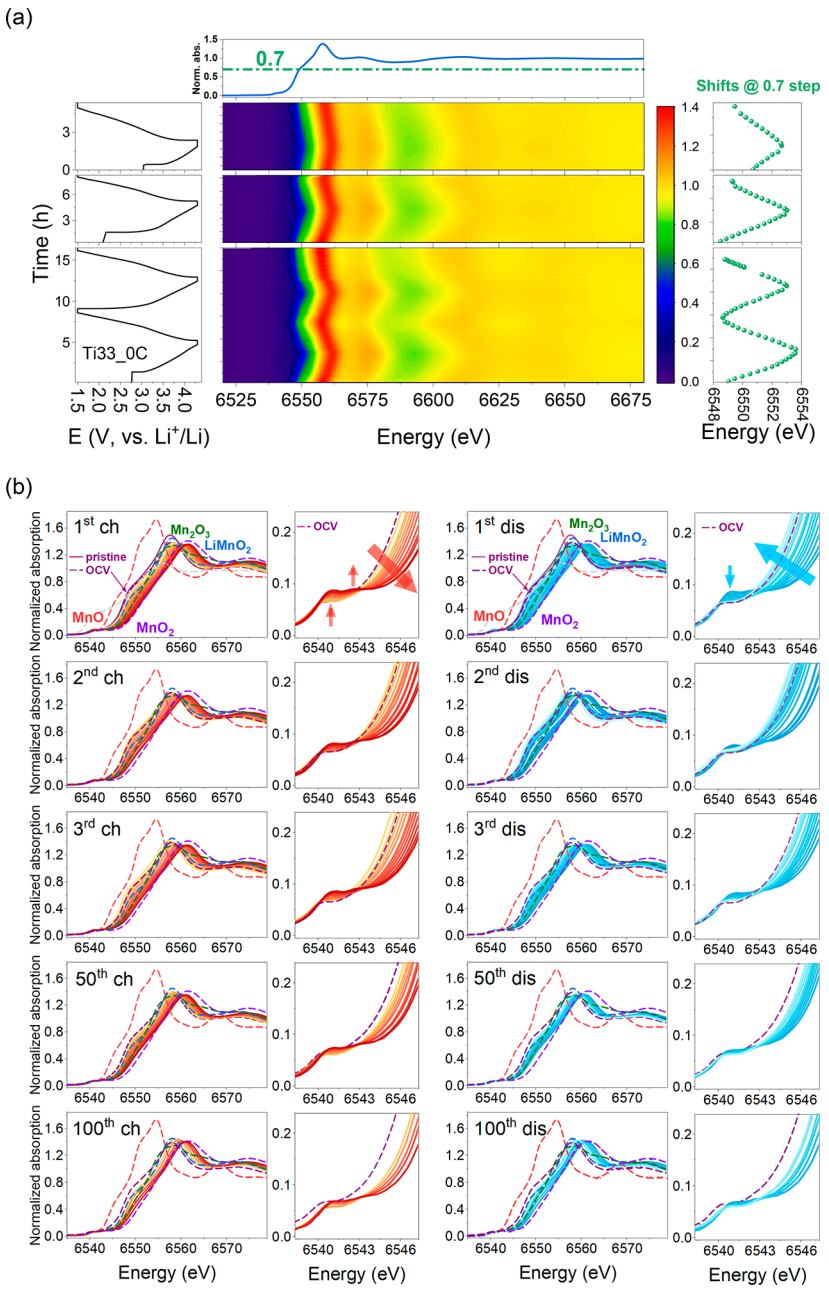

Figure 4. (a) Contour plot of normalized Mn *K*-edge spectra from the Ti33_0C electrode. The chemical shift is highlighted by the variation of energy position from the point corresponding to the 0.7 edge step on the rising edge. (b) Normalized Mn *K*-edge XANES of the fresh Ti33 electrode from the 1st to 3rd cycles and precycled electrodes for the 50th and 100th. The enlarged pre-edge regions shown on the right of the charge (ch) and discharge (dis) illustrate the 1*s*−3*d* quadrupole transition. Dashed lines represent the standard references $Mn^{2+}O$, $Mn^{3+}{}_2O_3$, $LiMn^{3+}O_2$, and $Mn^{4+}O_2$. The solid purple line represents the pristine Ti33 while the dashed purple line was measured on the as-assembled fresh electrode at OCV (2.77 V) before cycling. The darker/lighter color in the XANES spectra represents higher/lower voltage, respectively.

3.2. *Operando* Mn *K*-edge XAS of Ti33. *Operando* Mn *K*-edge XAS measurements were carried out for Ti33 ($Li_2Mn_{0.66}Ti_{0.33}O_2F$) on freshly prepared (Ti33_0C) and precycled (Ti33_49C and Ti33_99C for 49 and 99 cycles, respectively) electrodes with a cycling rate of C/10 (based on theoretical capacity) in the voltage window of 1.5−4.3 V. Figure 4a depicts the contour plots of normalized Mn *K*-edge spectra from the fresh electrode (Ti33_0C). A gradual cyclic shift of the edge toward higher/lower energy during charge (ch)/discharge (dis) was observed, as highlighted by the energy change of a point on the rising edge corresponding to 0.7 edge step, which showed a shift of ∼5 eV. This evolution represented the oxidation and reduction of Mn upon delithiation and lithiation, respectively; the shifts between Mn^{2+}, Mn^{3+}, and Mn^{4+} standards were in agreement with the $Mn^{2+/3+}/Mn^{3+/4+}$ double redox processes, as shown in the normalized XANES (Figure 4b). Consistently, the pre-edge peaks associated with the 1*s* → 3*d* quadrupole transitions also exhibited an intensity raise during charge (Mn oxidation) due to increased amount of available empty 3*d* states, which led to higher transition probability and more distinguishable splitting; an inverse trend was observed upon discharge. The Mn *K*-edge energy shifts evidenced the reversible Mn redox activities. However, we have noticed a shrinkage of the Mn redox range.

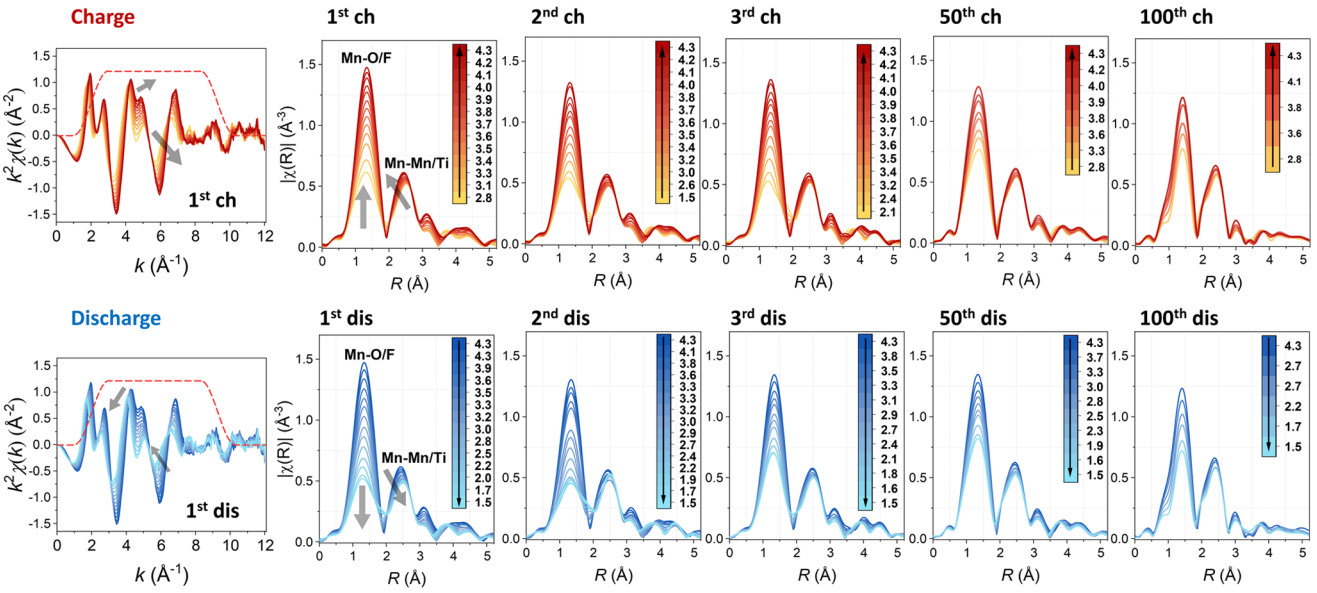

Figure 5. EXAFS spectra (presented in *R*-space) from *operando* Mn *K*-edge XAS measurements on the Ti33 electrodes recorded during various electrochemical cycles. The k^2-weighted $\chi(k)$ spectra of the first charge (ch)/discharge (dis) are exemplified on the leftmost panels; the red dashed lines represent the window function (Hanning window of dk = 2 Å^{-1}) for Fourier transform. The inset color scale bars with arrows indicate the direction of voltage change, and the numbers are the voltages at which the absorption spectra were recorded: yellow−orange−red → charge, dark blue−light blue → discharge. Darker/lighter color represents higher/lower voltage.

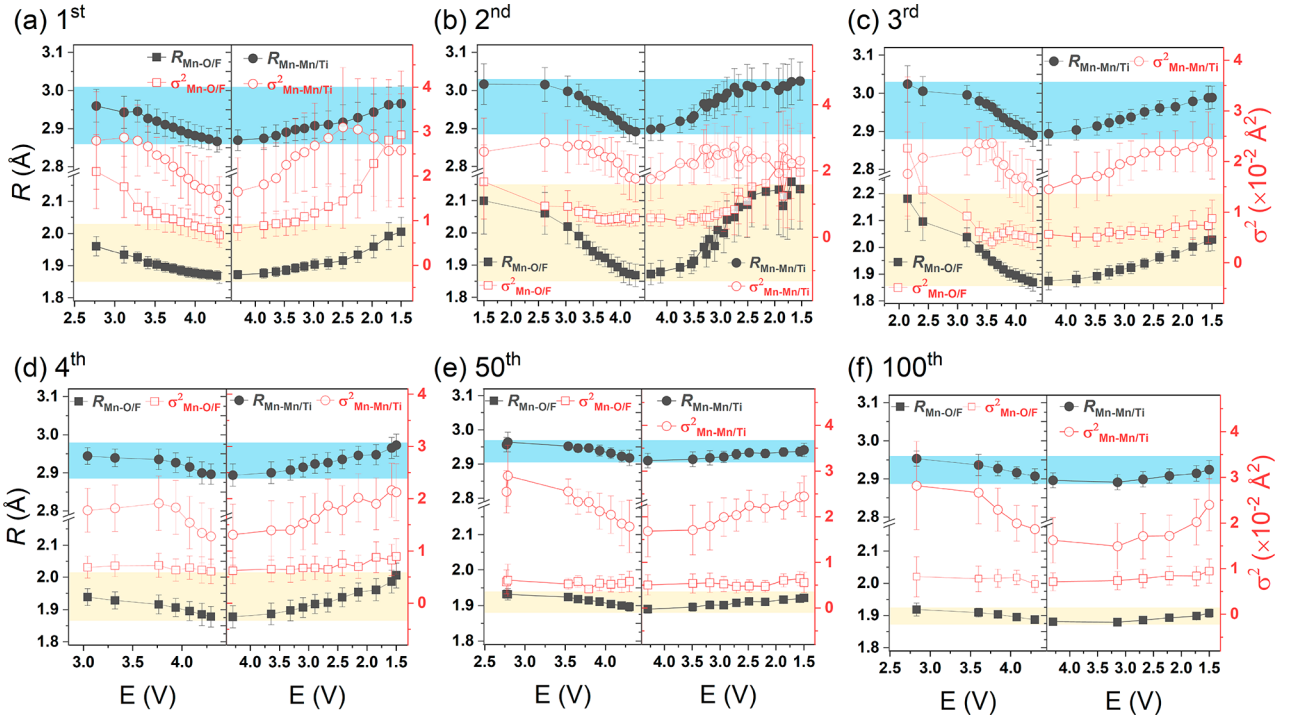

Figure 6. Parameters obtained from shell fitting of $|\chi(R)|$; from (a) to (d) the 1st−4th cycle of a fresh electrode, and (e) the 50th and (f) 100th cycle of precycled electrodes: *R* stands for the interatomic distance between the central absorbing Mn atoms and the first Mn−O/F coordination shell (■, $R_{Mn-O/F}$) as well as the second Mn−Mn/Ti coordination shell (●, $R_{Mn-Mn/Ti}$); σ^2 represents the mean-square relative displacement in *R* (structural disordering factor) for the Mn−O/F (□, $\sigma^2_{Mn-O/F}$) and Mn−Mn/Ti (○, $\sigma^2_{Mn-O/F}$).

In the fresh electrode, the Mn *K*-edge shifted between the pristine/OCV and MnO_2 indicating a change of oxidation states from the mixed 3+/2+ to approximately 4+. Upon prolonged cycling, the energy range of the edge shifts became narrower. Especially for the precycled electrodes, the formal Mn oxidation state in the discharged state (1.5 V) was prominently higher than that at the OCV of the fresh electrode (2.77 V, dashed purple lines).

The evolution of the Mn local structure upon charge/discharge during cycling was further probed by EXAFS as shown in Figure 5. For all cycles, the magnitude $|\chi(R)|$ of the Fourier transformed (FT) k^2-weighted $\chi(k)$ showed an increased amplitude during charging for both the first Mn−

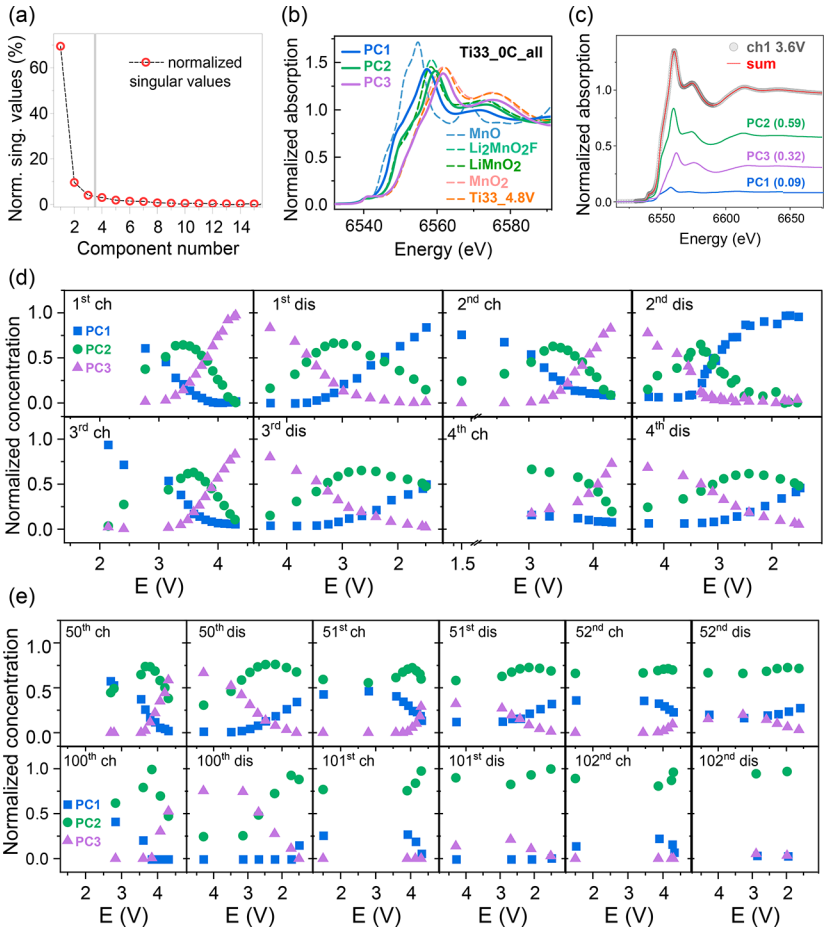

Figure 7. (a) Results (normalized singular values excluding the first component) of principal components analysis (PCA) based on normalized Mn *K*-edge spectra of Ti33_0C electrodes from the four initial cycles. (b) Constituent spectra representing the three pure components (PCs) obtained by MCR-ALS and their comparison with standards. (c) Example of an experimental spectrum (1st charge 3.6 V) represented by PCs with respective concentration fraction. (d) Concentration profiles of the Ti33 electrode: initial cycles (1st ch−4th dis) were obtained directly from MCR-ALS. (e) Extended cycles were received from a linear combination fit (LCF) using the pure spectra from (b) as components.

O/F and the second Mn−Mn/Ti coordination shells, resulting from the decreased local disordering upon the release of Li^+. Inversely, during discharge, reduced amplitudes were observed due to increased disordering by lithiation. Moreover, the $|\chi(R)|$ peaks representing the Mn−Mn/Ti shell showed an evident decrease (increase) in the average interatomic distance R upon delithiation (lithiation). This is in agreement with the lattice change observed by *ex-situ* XRD measurements in our previous work.[38]

The interatomic distances (R) between the central absorbing Mn and the first ($R_{Mn-O/F}$) and second ($R_{Mn-Mn/Ti}$) coordination shells were obtained through shell fitting, together with the disorder factor σ^2 (Figure 6). A simple model with two single-scattering paths was used to minimize the number of variables due to the limited data k range, as exemplified in Figure S5 and Table S3. In general, both $R_{Mn-O/F}$ and $R_{Mn-Mn/Ti}$ showed a decrease during charge and an increase upon discharge, indicating a local structure contraction with delithiation and expansion upon lithiation. The evolution of the first shell $R_{Mn-O/F}$ also agreed with the edge shifts probed by XANES, reflecting the inverse correlation between the bond length and formal oxidation state of the Mn in similar ligand coordination environment.[37,39] The disorder factor σ^2 showed similar evolution, though less representative compared to the amplitude change in Figure 5. The second Mn−Mn/Ti shell showed higher σ^2 values and larger variations with cycling because of Li insertion/extraction on these equivalent sites. Similar to the reduced shifts in edge energy within the 50th and 100th cycle, the $R_{Mn-O/F}$ and $R_{Mn-Mn/Ti}$ evolved in a narrower range (1.88−1.95 Å for $R_{Mn-O/F}$, 2.91−2.96 Å for $R_{Mn-Mn/Ti}$) compared to the initial cycles (1.86−2.20 Å for $R_{Mn-O/F}$, 2.88−3.02 Å for $R_{Mn-Mn/Ti}$).

During the Mn^{2+}/Mn^{3+} and Mn^{3+}/Mn^{4+} double redox processes of LMTOF materials upon cycling, intermediates with different Mn oxidation states may coexist, depending on the state of charge, and the measured absorption spectrum can be treated as a linear combination of such intermediates or transient constituents. The concentrations of these components to the averaged spectrum can be represented by experimental standards through linear combination fit (LCF), which is however limited by the choice of standard references.[23,40] Alternatively, principle component analysis (PCA) can mathematically determine the amount of intermediates in *operando* XAS data sets containing multiple spectra, and the independent components can be reconstructed as "pure spectra" through multivariate curve resolution by alternating least-squares (MCR-ALS).[41−43] In both cases, information about the intermediates that actively participate in the complex reactions and the general trends can be extracted. Figure 7a shows the normalized singular value against the

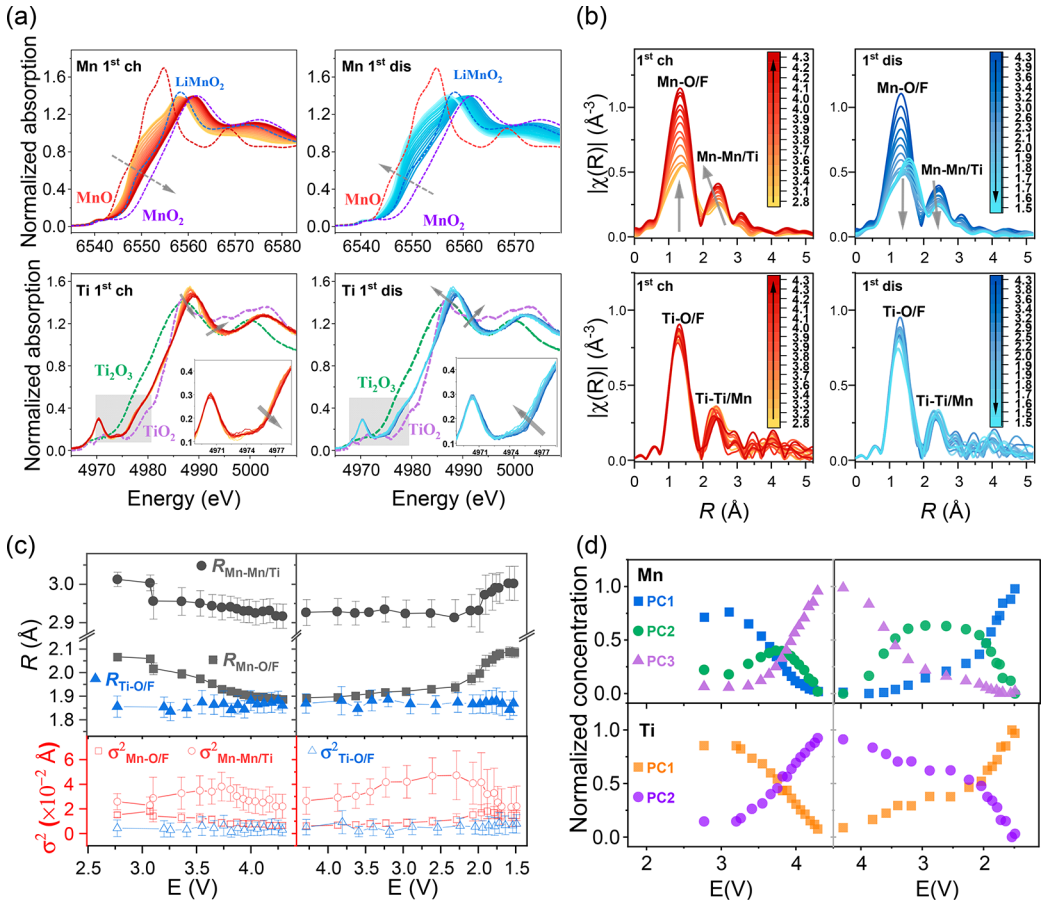

Figure 8. (a) Normalized Mn and Ti *K*-edge XANES results of fresh Ti66 electrode during the first charge (ch)−discharge (dis) cycle; arrows indicate the direction of edge shifts; dashed lines represent the standard references. (b) Corresponding Fourier transform of k^2-weighted $\chi(k)$ EXAFS. Darker (lighter) color represents higher (lower) voltage. The inset color scale bars with arrows indicate the direction of voltage change, and the numbers are the voltage at which the absorption spectra were recorded: yellow−orange−red → charge, dark blue−light blue → discharge. (c) EXAFS shell fitting using two paths (Mn−O/F and Mn−Mn/Ti) for Mn while only the first coordination shell (Ti−O/F) was included for Ti: R − interatomic distance from the central absorbing Mn or Ti atom to the neighboring atoms within the coordination shell, σ^2 − disordering factor. (d) Normalized concentration profiles obtained by MCR-ALS using three PCs for Mn and two PCs for Ti.

component number obtained from PCA based on the spectra collected from the fresh Ti33_0C electrode without the first component to exclude the variance contribution of the edge-jump. Apart from the first and second points with major contributions, the third one represented about 4% of the sum of all singular values and seemed in trend with the remaining data points reaching a minimum close to zero. Therefore, we concluded that three components in total incorporated the majority of the structural information in this data matrix, in agreement with our prior knowledge of the system with Mn double redox. Accordingly, three pure components were taken into account in MCR-ALS and their "pure spectra" (PCs) were extracted from the initial cycles (1st−4th) of the fresh Ti33_0 electrode. These pure spectra showed distinct edge shifts and were attributed to three Mn intermediate states (Figure 7b). Compared to the experimental standards, PC2 was close to $LiMn^{3+}O_2$ and $Li_2Mn^{3+}O_2F$—both were laboratory synthesized with the same DRS structure as LMTOF and XPS confirmed their Mn^{3+} valence state. PC3 showed an edge energy close to that of $Mn^{4+}O_2$ as well as the overcharged Ti33 electrode (Ti33_4.8 V), in which Mn was oxidized to 4+. A larger discrepancy was observed between PC1 and $Mn^{2+}O$, most likely due to the fact that Mn in LMTOF could not be completely reduced to Mn^{2+} and PC1 represented a mixed $Mn^{2+/3+}$ valence.

Furthermore, the experimental spectra were reconstructed as a linear combination of these PCs with their respective concentration fractions, as exemplified in Figure 7c with more details in Figure S6 and Figure S7. Accordingly, Figure 7d shows the development of percentages of these three components for the fresh Ti33_0C electrode during the four initial cycles. Taking the first charge as an example: from OCV with a mixture of PC1+PC2, the concentration of PC1 decreased while PC2 increased. Above 3 V, PC3 that represents the highest Mn oxidation state emerged, and PC2 reached an inflection point, after which it started to decrease together with PC1. At even higher voltages, the fraction of PC3 surpassed PC2 (intersection of both curves) and eventually became predominant at a fully charged state (4.3 V) with a weight close to unity. This variation demonstrated a transition process during charge as PC1 → PC2 → PC3, which corresponded to the oxidation of Mn as $LM^{2+/3+}TOF$ → $LM^{3+}TOF$ → $LM^{4+}TOF$ upon delithiation. During the subsequent discharge, a reverse trend was observed, where PC1 dominated at 1.5 V revealing that Mn was more reduced in the discharged state then at the OCV. These reversible interchanges between the components reflected the Mn^{2+}/

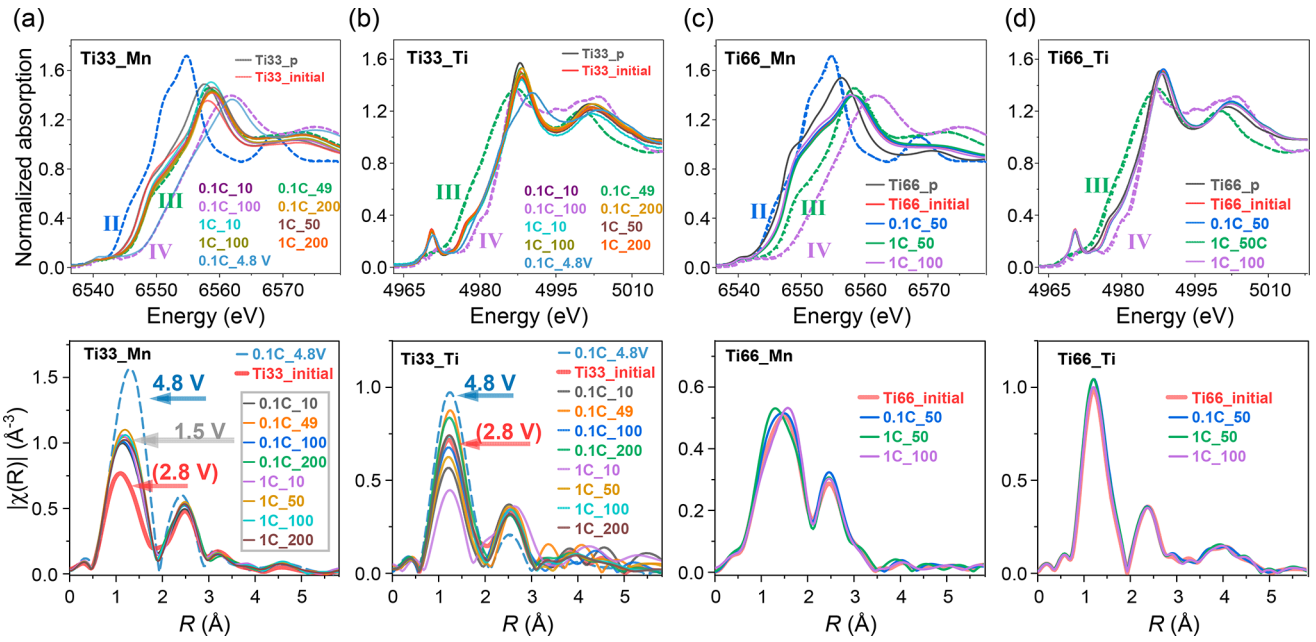

Figure 9. Normalized XANES spectra at Mn and Ti *K*-edge spectra from discharged Ti33 (a, b) and Ti66 (c, d) electrode tapes measured *ex-situ*: as-prepared tapes without cycling (Ti33_ and Ti66_initial) and tapes cycled at 1C and 0.1C rate until 10, 49, 50, 100, or 200 cycles, respectively. Spectra from pristine materials (Ti33_p and Ti66_P) and one charged Ti33 electrode cycled to high voltage at C/10 (0.1C_4.8 V) are compared. The lower graphs show the corresponding Fourier transform $|\chi(R)|$ of k^2-weighted $\chi(k)$.

Mn^{3+} and Mn^{3+}/Mn^{4+} double redox reactions during the electrochemical cycling. In general, a similar evolution was observed during the four initial cycles. However, it is worth noting that the extent of variations was gradually reduced with cycling. During the first two cycles, an almost full concentration (~100%) of PC3 was obtained at 4.3 V while PC1 dominated in the discharged state at 1.5 V. In the third and fourth cycles, a small amount of PC2 was not oxidized to PC3 at 4.3 V resulting in mixed PC2+PC3 components. Moreover, a considerable fraction of PC2 was still observed in the discharged states with a comparable concentration with respect to PC1. This phenomenon became more prominent after extended cycling of the precycled electrodes (Figure 7e), especially after the first (50th and 100th) cycle. We noticed a drastically reduced variation among the three components, and PC2 eventually became predominant regardless of the voltage. In agreement with the reduced Mn chemical shifts probed by XANES, the concentration variation also indicated a degradation of the Mn double-redox activity.

For comparison, linear combination fit (LCF) was also performed using experimental spectra measured from $Mn^{2+}O$, $LiMn^{3+}O_2$, and $Mn^{4+}O_2$ standards (Figure S8a). In this study, laboratory synthesized $LiMnO_2$ was used as Mn^{3+} standard thanks to the same DRS structure and similar coordination environment as in the LMTOF materials, and its 3+ oxidation state was confirmed by XPS (Figure S3) and XANES (Figure S4a). The results were more suggestive, as LMTOF in this study showed no intermediates corresponding to $Mn^{2+}O$, and thus the fitting uncertainties (reduced-χ^2) were large for the discharged states (Figure S9a). Nevertheless, the variation of component fractions obtained by LCF showed a comparable evolution as in MCR-ALS (Figure S10b,c). From OCV with a combination of Mn^{2+} and Mn^{3+}, the weight of Mn^{2+} deceased upon charging while that of Mn^{3+} increased as a result of the Mn^{2+}/Mn^{3+} redox, followed by the subsequent Mn^{3+}/Mn^{4+}redox at higher voltages with the appearance and growth of Mn^{4+}. This process was also reversible in discharge, and the mixture of 2+ and 3+ components at 1.5 V for the initial cycles could be correlated to the PC1. From the third discharge, Mn^{2+} showed much smaller weight (<0.1) in the discharged state as well as a reduced variation in the fourth cycle. After extended cycling (Figure S8c), the contribution of Mn^{2+} remained low in any state of charge. In accordance with MCR-ALS, with continuous cycling and degraded capacity, Mn^{3+} and Mn^{4+} became the main varying constituents, and the former was prevailing.

3.3. *Operando* Mn and Ti *K*-Edge XAS of Ti66. For the $Li_2Mn_{0.33}Ti_{0.66}O_2F$ (Ti66) electrode with a higher Ti concentration, both Mn and Ti *K*-edge *operando* XAS measurements were performed. Figure 8a,b shows the normalized XANES spectra and FT $|\chi(R)|$ of Ti66 during the first cycle. Similar to the Ti33 electrode, Ti66 exhibited a progressive Mn *K*-edge shift toward higher energy as well as an increasing amplitude of $|\chi(R)|$ during the charge, resulting from the Mn oxidation and the reduced local disordering upon delithiation; and vice versa for the discharge. Ti also exhibited small edge shifts (indicated by the gray arrows), which were more distinct during discharge over a wider voltage range (4.3−1.5 V). By comparing between the charged (4.3 V) and discharged (1.5 V) states, a small shift of the pre-edge peak (~0.12 eV) to lower energy and a slight decrease of peak intensity were observed (Figure S11). These modifications can be mainly attributed to a local structure change of Ti upon lithiation and delithiation.[44,45] As observed in $|\chi(R)|$, Ti showed relatively weaker amplitude variation, suggesting that the Ti local environment was less influenced by lithium release and uptake compared to Mn. This was also supported by the shell fitting shown in Figure 8c. The distance from a central Ti atom to the O/F ligands $R_{Ti-O/F}$ showed only negligible changes upon charge−discharge, while a more pronounced evolution in $R_{Mn-O/F}$ was observed for Mn. Compared to Ti33,

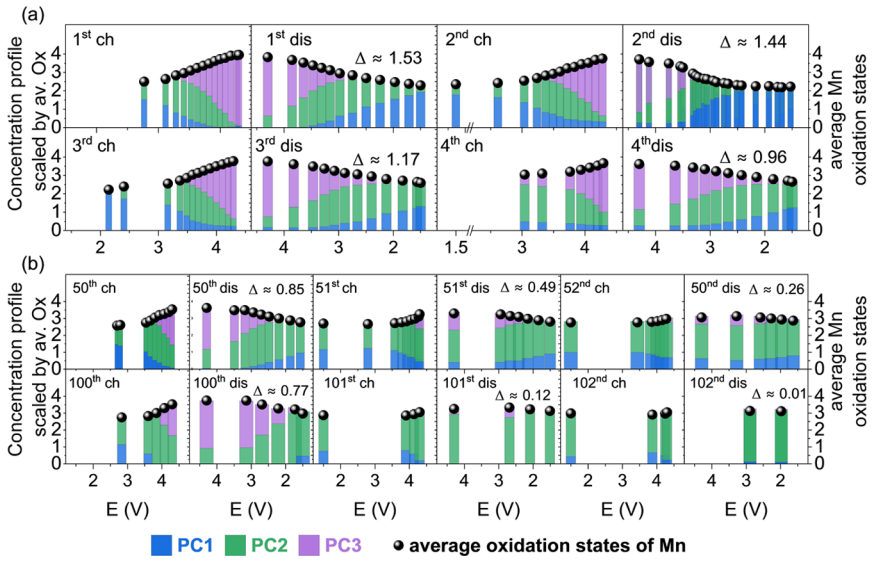

Figure 10. Concentration profile of pure components scaled by the average Mn oxidation states for fresh Ti33_0C (a) and precycled Ti33_49C and Ti33_99C (b) electrodes. Blue, green, and violet columns represent the PC1, PC2, and PC3 in Figure 7 scaled by the calculated average Mn oxidation states (black spheres). Δ shows the change of average Mn oxidation states during discharge.

Ti66 showed overall lower Mn oxidation states as well as larger $R_{Mn-O/F}$ (1.89–2.06 Å, vs 1.86–2.02 Å for Ti33).

MCR-ALS was also performed for Ti66. Three pure components were extracted for Mn and the concentration profile (Figure 8d) evidenced the Mn double redox. However, it is worth noting that these pure spectra (PCs) were not the same as for Ti33 and, in general, exhibited lower edge energy (Figure S10a). Therefore, a more straightforward comparison between Ti33 and Ti66 was made by LCF based on the same experimental standards (Figure S10b). From the component variation during the first cycle, the Mn^{2+} in Ti66 (solid symbols) showed higher weight at all voltages, while the higher-valent Mn^{3+} and Mn^{4+} were present with reduced fractions in comparison with those in Ti33 (open symbols). This was probably due to the predominant amount of low-valent Mn^{2+} in pristine Ti66 in favor of the Mn^{2+}/Mn^{3+} redox couple in the initial cycles. For Ti, the two pure components PC1 and PC2 obtained from MCR-ALS were attributed to two distinct local environments for Ti between the charged and discharged state. As EXAFS showed distinct variation in $|\chi(R)|$ amplitude but no prominent changes in $R_{Ti-O/F}$, it is likely due to a rearrangement of coordination atoms rather than any distortion of octahedra.

3.4. *Ex-Situ* XAS on Precycled Electrodes. Ti33 and Ti66 electrodes cycled at different rates and up to various cycles were also compared using electrode tape measured *ex-situ*, as shown in Figure 9. For Ti33, all discharged electrodes showed a slight shift of the Mn *K*-edge toward higher energy in comparison to the pristine (Ti33_p) and the uncycled electrode (Ti33_initial) regardless of the charge–discharge rate and the cycle number (Figure 9a, upper). To represent the delithiated state for comparison, an electrode that was charged to 4.8 V (0.1C_4.8 V) was also investigated, which showed a Mn *K*-edge approaching that of $Mn^{4+}O_2$. The Fourier transform $|\chi(R)|$ showed distinct Mn coordination environments between the state of charge (Figure 9a, lower): all discharged electrodes (1.5 V) exhibited similar amplitudes for the first coordination shell, which were stronger than that of the uncycled Ti33_initial (OCV ≈ 2.8 V) but weaker than the fully charged electrode (4.8 V). For Ti, no prominent Ti *K*-edge shift was observed (Figure 9b, top), except for the overcharged 0.1C_4.8 V sample. Unlike for Mn, the $|\chi(R)|$ for the first Ti–O/F shell could not be categorized by the state of charge, probably due to the redox inactivity of Ti in Ti33. Moreover, the large and random variation in $|\chi(R)|$ amplitudes might suggest a strong modulation of the Ti local structure by Li insertion–extraction. This is in agreement with a previous Raman study on Ti33, where it was found that Li had a tendency to insert into sites close to Ti favoring the TiO_6 and LiF_6 coordination.[38] With cycling going on, such site-selective occupancy could lead to a continuous change of the Ti local environment and a strong deviation from the initial structure.

Similarly, all discharged Ti66 electrodes showed increased Mn oxidation states (Figure 9c, top) compared to the pristine materials (Ti66_p). In addition, a slight shift of the Ti *K*-edge was observed (Figure 9d, upper) for all cycled electrodes, indicating an irreversible local structural modification from the initial state. Moreover, no prominent variation was observed in $|\chi(R)|$ for Mn and Ti (Figure 9c,d, lower), implying similar local environments in discharged states after long cycles.

In summary, Ti33 electrodes cycled over 1.5–4.3 V showed a predominant redox contribution from Mn without an evident Ti redox activity. After long cycling, the higher Mn oxidation state with decreased local disordering in the discharged state might suggest an increasingly hindered lithation, preventing the electrode from reverting to its initial status. For Ti66, a relatively more stable local structure subject to lithiation–delithiation cycling was observed.

3.5. Discussion. So far, the capacity loss in Li-rich Mn based cathode materials has usually been attributed to oxygen loss, Mn dissolution into electrolytes, and/or irreversible structure changes.[19,46] For the DRS LMTOF materials system, the DEMS results evidenced that the Ti substitution successfully stabilized the electrode with respect to lattice oxygen loss, and the overall extent of oxygen loss from these materials was very small even with higher cutoff voltage (1.5–4.8 V). Therefore, for the selected Ti33 and Ti66 electrode cycled in a voltage window of 1.5–4.3 V, oxygen loss was

considered as neither a primary mechanism for the capacity degradation after prolonged cycling nor an affecting factor for the oxidation states and local structure of the redox-active transition metals.

From the *operando* XAS results of Ti33 electrodes, we observed declining Mn *K*-edge shifts in XANES as well as a reduced variation of pure components derived from MCR-ALS and LCF after prolonged cycling, evidencing a gradual degradation of the Mn double-redox activity that was most likely responsible for the capacity degradation. Assuming Mn is the only redox-active transition metal and Ti remains +4, it is possible to reconstruct the composition of Ti33 on an indicative basis using the fraction of pure components at OCV. By arbitrarily assigning PC2 as Mn^{3+} and PC3 as Mn^{4+}, the oxidation state of PC1 was obtained as $Li_2Mn^{2.152+}_{PC1}Mn^{3+}_{PC2}Mn^{4+}_{PC3}O_2F$, which is equivalent to the nominal composition $Li_2Mn_{2/3}{}^{2.5+}Ti^{4+}{}_{1/3}O_2F$. Based on the concentration profiles (Figure 7), the average Mn oxidation states (av. Ox) can be simulated by 2.152 × PC1 + 3 × PC2 + 4 × PC7 as shown in Figure 10. From the initial cycle, the variation of average Mn oxidation states (Δ) between the charged and discharged states showed a gradual decrease, from ca. 1.53 in the first discharge to 0.96 in the fourth discharge and significantly lower in extended cycles (50th dis and 100th dis). If Ti is considered stable at +4 and oxygen redox is not taken into account, the charge compensation becomes solely based on Mn reduction during lithiation; the lower and lower Δ upon cycling can be directly correlated to the observed decrease of the discharge capacity. Moreover, the reduced height changes between the PC1, PC2, and PC3 columns can also reflect the gradual loss of Mn redox activity, in accordance with the decreased Mn edge shifts and reduced local structure evolution, as well as the resulting capacity degradation (Figure S12).

For Ti33, the local structure change of Mn probed by EXAFS revealed distinct variations in the interatomic distance and disorder parameters in the initial cycles. After prolonged cycling, though a similar radial distribution in the Fourier transformed $|\chi(R)|$ evidenced no drastic structure change such as a phase transition, the reduced variation in the Mn−O/F bond length and in the amplitude of the Mn−Mn/Ti coordination shell suggest an increased local ordering with decreased reversibility for the Li incorporation. The capability of reversibly accommodating the Li insertion−extraction was no longer preserved. Consistently, from the *ex-situ* measurements, all discharged electrodes demonstrated convergent characteristics for Mn with an average oxidation state close to Mn^{3+} as well as a general increase of local ordering compared to pristine materials. This might result from the site-selective occupancy and preferential coordination as shown in our previous Raman study on LMTOF, which also detected an overall symmetry deviation from a simple DRS structure upon cycling.[38] Moreover, it is worth noting that Mn^{3+} is more vulnerable to the Jahn−Teller distortion due to the odd electron on e_g ($t_{2g}{}^3e_g{}^1$).[47] Partial fluorination can mitigate the Jahn−Teller distortion and thus improve the Mn redox.[31] However, this benefit would be compromised if more Mn became coordinated as $Mn^{3+}O_6$ instead of $Mn^{2+/3+}O_{6-y}F_y$ throughout the long cycling due to increased short-range order.[48]

4. CONCLUSION

In this work, synchrotron *operando* XAS was applied to understand the chemical and local structure evolution of a representative class of Mn-based disordered rocksalt cathode materials, $Li_2Mn_{1-x}TixO_2F$ (LMTOF, $0 \leq x \leq 2/3$), upon electrochemical cycling. For $Li_2Mn_{0.66}Ti_{0.33}O_2F$ (Ti33), Mn *K*-edge XANES and EXAFS confirmed the reversible Mn double redox activities in the initial cycles, which successively degraded in longer cycles, as reflected by a smaller variation in oxidation state and bond-length. Both MCR-ALS and LCF analyses showed a reduction of the Mn component with the lowest oxidation state, indicating the disappearance of Mn^{2+}/Mn^{3+} redox activity with prolonged cycling. In the case of $Li_2Mn_{0.33}Ti_{0.66}O_2F$ (Ti66), similar redox behavior was found for Mn and a cycling-induced local structure modification was observed for Ti in the initial cycle. The comparison of LCF indicated that the larger content of Ti might attenuate the presence of Mn^{3+}/Mn^{4+} in favor of the Mn^{2+}/Mn^{3+} redox couple. EXAFS evidenced cycling-induced local structure changes for Mn and a rather stable coordination environment for Ti. *Ex-situ* XAS on cycled Ti33 and Ti66 electrodes revealed a similar higher Mn oxidation state in the discharged state compared to the pristine materials, independent of cycle number and charge−discharge rate. In summary, the gradual alteration of Mn double-redox activity with prolonged cycling is considered responsible for the capacity degradation associated with the cycling-induced irreversible local ordering. For further development of these DRS oxyfluoride cathodes, optimization of the cycling stability with a more precise control over the cations' local environment can be envisaged.

AUTHOR INFORMATION

Corresponding Author

Yang Hu − *Helmholtz Institute Ulm (HIU), 89081 Ulm, Germany*; orcid.org/0000-0001-6864-6498; Email: yang.hu@kit.edu

Authors

Yasaman Shirazi Moghadam − *Helmholtz Institute Ulm (HIU), 89081 Ulm, Germany*

Abdel El Kharbachi − *Helmholtz Institute Ulm (HIU), 89081 Ulm, Germany*; orcid.org/0000-0003-4332-1544

Stéphanie Belin − *Synchrotron SOLEIL, L'Orme des Merisiers, 91190 Saint-Aubin, France*

Thomas Diemant − *Helmholtz Institute Ulm (HIU), 89081 Ulm, Germany*

Jun Chen − *Departments of Materials, University of Oxford, Oxford OX1 3PH, U.K.*

Robert A. House − *Departments of Materials, University of Oxford, Oxford OX1 3PH, U.K.;* orcid.org/0000-0002-7415-477X

Peter G. Bruce − *Departments of Materials, University of Oxford, Oxford OX1 3PH, U.K.;* orcid.org/0000-0001-6748-3084

Maximilian Fichtner − *Helmholtz Institute Ulm (HIU), 89081 Ulm, Germany; Institute of Nanotechnology, Karlsruhe Institute of Technology (KIT), 76021 Karlsruhe, Germany;* orcid.org/0000-0002-7127-1823

Author Contributions

The manuscript was written through contributions of all authors. All authors have given approval to the final version of the manuscript.

Notes

The authors declare no competing financial interest.

ACKNOWLEDGMENTS

This work contributes to the research performed at CELEST (Center for Electrochemical Energy Storage Ulm-Karlsruhe) and was partially funded by the German Research Foundation (DFG) under Project ID 390874152 (POLiS Cluster of Excellence). The synchrotron studies of this work at the ROCK beamline of SOLEIL (proposal number 20210779) were supported by a public grant overseen by the French National Research Agency (ANR) as part of the "Investissements d'Avenir" program (reference: ANR-10-EQPX-45). The TEM characterization experiments were performed at the Karlsruhe Nano Micro Facility (KNMF), Helmholtz research infrastructure operated at KIT. Y.S.M. and A.E. thank G. Melinte for assistance in the TEM analysis.

REFERENCES

(1) Whittingham, M. S. Lithium batteries and cathode materials. *Chem. Rev.* **2004**, *104* (10), 4271−301.

(2) Lee, J.; Urban, A.; Li, X.; Su, D.; Hautier, G.; Ceder, G. Unlocking the potential of cation-disordered oxides for rechargeable lithium batteries. *Science* **2014**, *343* (6170), 519−22.

(3) Goodenough, J. B.; Abruna, H. D.; Buchanan, M. V. *Basic Research Needs for Electrical Energy Storage. Report of the Basic Energy Sciences Workshop on Electrical Energy Storage, April 2−4, 2007*; Office of Science, U.S. Department of Energy: 2007.

(4) Yabuuchi, N.; Takeuchi, M.; Nakayama, M.; Shiiba, H.; Ogawa, M.; Nakayama, K.; Ohta, T.; Endo, D.; Ozaki, T.; Inamasu, T.; Sato, K.; Komaba, S. High-capacity electrode materials for rechargeable lithium batteries: Li3NbO4-based system with cation-disordered rocksalt structure. *Proc. Natl. Acad. Sci. U. S. A.* **2015**, *112* (25), 7650−5.

(5) Liu, H.; Zhu, Z.; Yan, Q.; Yu, S.; He, X.; Chen, Y.; Zhang, R.; Ma, L.; Liu, T.; Li, M.; Lin, R.; Chen, Y.; Li, Y.; Xing, X.; Choi, Y.; Gao, L.; Cho, H. S.; An, K.; Feng, J.; Kostecki, R.; Amine, K.; Wu, T.; Lu, J.; Xin, H. L.; Ong, S. P.; Liu, P. A disordered rock salt anode for fast-charging lithium-ion batteries. *Nature* **2020**, *585* (7823), 63−67.

(6) Diaz-Lopez, M.; Chater, P. A.; Joly, Y.; Proux, O.; Hazemann, J.-L.; Bordet, P.; Pralong, V. Reversible densification in nano-Li 2 MnO 3 cation disordered rock-salt Li-ion battery cathodes. *Journal of Materials Chemistry A* **2020**, *8* (21), 10998−11010.

(7) Blumenhofer, I.; Shirazi Moghadam, Y.; El Kharbachi, A.; Hu, Y.; Wang, K.; Fichtner, M. Synthesis and Structure Stabilization of Disordered Rock Salt Mn/V-Based Oxyfluorides as Cathode Materials for Li-Ion Batteries. *Acs Materials Au* **2023**, *3* (2), 132−142.

(8) Chen, R.; Ren, S.; Knapp, M.; Wang, D.; Witter, R.; Fichtner, M.; Hahn, H. Disordered Lithium-Rich Oxyfluoride as a Stable Host for Enhanced Li+Intercalation Storage. *Adv. Energy Mater.* **2015**, *5* (9), 1401814.

(9) Rosy; Sclar, H.; Evenstein, E.; Haber, S.; Maiti, S.; Sharabani, T.; Leskes, M.; Noked, M. Mitigating Structural Instability of High-Energy Lithium-and Manganese-Rich LiNi x Mn y Co z Oxide by Interfacial Atomic Surface Reduction. *Chem. Mater.* **2019**, *31* (10), 3840−3847.

(10) Pimenta, V.; Sathiya, M.; Batuk, D.; Abakumov, A. M.; Giaume, D.; Cassaignon, S.; Larcher, D.; Tarascon, J. M. Synthesis of Li-Rich NMC: A Comprehensive Study. *Chem. Mater.* **2017**, *29* (23), 9923−9936.

(11) Shirazi Moghadam, Y.; El Kharbachi, A.; Diemant, T.; Melinte, G.; Hu, Y.; Fichtner, M. Toward Better Stability and Reversibility of the Mn4+/Mn2+ Double Redox Activity in Disordered Rocksalt Oxyfluoride Cathode Materials. *Chem. Mater.* **2021**, *33* (21), 8235−8247.

(12) Shirazi Moghadam, Y.; El Kharbachi, A.; Cambaz, M. A.; Dinda, S.; Diemant, T.; Hu, Y.; Melinte, G.; Fichtner, M. Borate-Based Surface Coating of Li-Rich Mn-Based Disordered Rocksalt Cathode Materials. *Advanced Materials Interfaces* **2022**, *9* (35), 2201200.

(13) Shirazi Moghadam, Y.; El Kharbachi, A.; Melinte, G.; Diemant, T.; Fichtner, M. Bulk and Surface Stabilization Process of Metastable Li-Rich Disordered Rocksalt Oxyfluorides as Efficient Cathode Materials. *J. Electrochem. Soc.* **2022**, *169* (12), 120514.

(14) Luo, K.; Roberts, M. R.; Hao, R.; Guerrini, N.; Pickup, D. M.; Liu, Y. S.; Edstrom, K.; Guo, J. H.; Chadwick, A. V.; Duda, L. C.; Bruce, P. G. Charge-compensation in 3d-transition-metal-oxide intercalation cathodes through the generation of localized electron holes on oxygen. *Nat. Chem.* **2016**, *8* (7), 684−691.

(15) Luo, K.; Roberts, M. R.; Guerrini, N.; Tapia-Ruiz, N.; Hao, R.; Massel, F.; Pickup, D. M.; Ramos, S.; Liu, Y. S.; Guo, J.; Chadwick, A. V.; Duda, L. C.; Bruce, P. G. Anion Redox Chemistry in the Cobalt Free 3d Transition Metal Oxide Intercalation Electrode Li-[Li0.2Ni0.2Mn0.6]O2. *J. Am. Chem. Soc.* **2016**, *138* (35), 11211−8.

(16) Daniel, C.; Mohanty, D.; Li, J.; Wood, D. L. *Cathode materials review*; American Institute of Physics: 2014; Vol. *1597*, pp 26−43.

(17) Komaba, S.; Kumagai, N.; Sasaki, T.; Miki, Y. Manganese dissolution from lithium doped Li-Mn-O spinel cathode materials into electrolyte solution. *Electrochemistry* **2001**, *69* (10), 784−787.

(18) Amatucci, G.; Tarascon, J. M. Optimization of Insertion Compounds Such as LiMn[sub 2]O[sub 4] for Li-Ion Batteries. *J. Electrochem. Soc.* **2002**, *149* (12), K31.

(19) Sharpe, R.; House, R. A.; Clarke, M. J.; Förstermann, D.; Marie, J.-J.; Cibin, G.; Zhou, K.-J.; Playford, H. Y.; Bruce, P. G.; Islam, M. S. Redox Chemistry and the Role of Trapped Molecular O2 in Li-Rich Disordered Rocksalt Oxyfluoride Cathodes. *J. Am. Chem. Soc.* **2020**, *142* (52), 21799−21809.

(20) Lee, J.; Kitchaev, D. A.; Kwon, D. H.; Lee, C. W.; Papp, J. K.; Liu, Y. S.; Lun, Z.; Clement, R. J.; Shi, T.; McCloskey, B. D.; Guo, J.; Balasubramanian, M.; Ceder, G. Reversible Mn(2+)/Mn(4+) double redox in lithium-excess cathode materials. *Nature* **2018**, *556* (7700), 185−190.

(21) La Fontaine, C.; Belin, S.; Barthe, L.; Roudenko, O.; Briois, V. ROCK: A Beamline Tailored for Catalysis and Energy-Related Materials from ms Time Resolution to μm Spatial Resolution. *Synchrotron Radiation News* **2020**, *33* (1), 20−25.

(22) Briois, V.; La Fontaine, C.; Belin, S.; Barthe, L.; Moreno, T.; Pinty, V.; Carcy, A.; Girardot, R.; Fonda, E. ROCK: the new Quick-EXAFS beamline at SOLEIL. *Journal of Physics: Conference Series* **2016**, *712*, 012149.

(23) Leriche, J. B.; Hamelet, S.; Shu, J.; Morcrette, M.; Masquelier, C.; Ouvrard, G.; Zerrouki, M.; Soudan, P.; Belin, S.; Elkaim, E.; Baudelet, F. An Electrochemical Cell for Operando Study of Lithium Batteries Using Synchrotron Radiation. *J. Electrochem. Soc.* **2010**, *157* (5), A606−A610.

(24) Landrot, G. FASTOSH: a software to process XAFS data for geochemical & environmental applications. In *Abstracts, Goldschmidt 2018 conference*; Goldschmidt: Boston, 2018; p 1402.
(25) Ravel, B.; Newville, M. ATHENA, ARTEMIS, HEPHAESTUS: data analysis for X-ray absorption spectroscopy using IFEFFIT. *J. Synchrotron Radiat* **2005**, *12* (4), 537−41.
(26) Newville, M. Larch: An Analysis Package for XAFS and Related Spectroscopies. *Journal of Physics: Conference Series* **2013**, *430*, 012007.
(27) Newville, M.; Livins, P.; Yacoby, Y.; Rehr, J. J.; Stern, E. A. Near-edge x-ray-absorption fine structure of Pb: A comparison of theory and experiment. *Phys. Rev. B Condens Matter* **1993**, *47* (21), 14126−14131.
(28) Newville, M. EXAFS analysis using FEFF and FEFFIT. *J. Synchrotron Radiat* **2001**, *8* (2), 96−100.
(29) Maitra, U.; House, R. A.; Somerville, J. W.; Tapia-Ruiz, N.; Lozano, J. G.; Guerrini, N.; Hao, R.; Luo, K.; Jin, L.; Perez-Osorio, M. A.; Massel, F.; Pickup, D. M.; Ramos, S.; Lu, X.; McNally, D. E.; Chadwick, A. V.; Giustino, F.; Schmitt, T.; Duda, L. C.; Roberts, M. R.; Bruce, P. G. Oxygen redox chemistry without excess alkali-metal ions in Na(2/3)[Mg(0.28)Mn(0.72)]O(2). *Nat. Chem.* **2018**, *10* (3), 288−295.
(30) Tapia-Ruiz, N.; Soares, C.; Somerville, J. W.; House, R. A.; Billaud, J.; Roberts, M. R.; Bruce, P. G. P2-Na2/3Mg1/4Mn7/12Co1/6O2 cathode material based on oxygen redox activity with improved first-cycle voltage hysteresis. *J. Power Sources* **2021**, *506*, 230104.
(31) Lun, Z. Y.; Ouyang, B.; Kitchaev, D. A.; Clement, R. J.; Papp, J. K.; Balasubramanian, M.; Tian, Y. S.; Lei, T.; Shi, T.; McCloskey, B. D.; Lee, J.; Ceder, G. Improved Cycling Performance of Li-Excess Cation-Disordered Cathode Materials upon Fluorine Substitution. *Adv. Energy Mater.* **2019**, *9* (2), 1802959.
(32) Kan, W. H.; Chen, D. C.; Papp, J. K.; Shukla, A. K.; Huq, A.; Brown, C. M.; McCloskey, B. D.; Chen, G. Y. Unravelling Solid-State Redox Chemistry in Li1.3Nb0.3Mn0.4O2 Single-Crystal Cathode Material. *Chem. Mater.* **2018**, *30* (5), 1655−1666.
(33) Luo, M.; Zheng, S.; Wu, J.; Zhou, K.; Zuo, W.; Feng, M.; He, H.; Liu, R.; Zhu, J.; Zhao, G.; Chen, S.; Yang, W.; Peng, Z.; Wu, Q.; Yang, Y. Identifying the anionic redox activity in cation-disordered Li1.25Nb0.25Fe0.50O2/C oxide cathodes for Li-ion batteries. *Journal of Materials Chemistry A* **2020**, *8* (10), 5115−5127.
(34) Castel, E.; Berg, E. J.; El Kazzi, M.; Novák, P.; Villevieille, C. Differential Electrochemical Mass Spectrometry Study of the Interface of xLi2MnO3·(1-x)LiMO2 (M = Ni, Co, and Mn) Material as a Positive Electrode in Li-Ion Batteries. *Chem. Mater.* **2014**, *26* (17), 5051−5057.
(35) Strehle, B.; Kleiner, K.; Jung, R.; Chesneau, F.; Mendez, M.; Gasteiger, H. A.; Piana, M. The Role of Oxygen Release from Li- and Mn-Rich Layered Oxides during the First Cycles Investigated by On-Line Electrochemical Mass Spectrometry. *J. Electrochem. Soc.* **2017**, *164* (2), A400−A406.
(36) Luo, K.; Roberts, M. R.; Hao, R.; Guerrini, N.; Pickup, D. M.; Liu, Y. S.; Edstrom, K.; Guo, J.; Chadwick, A. V.; Duda, L. C.; Bruce, P. G. Charge-compensation in 3d-transition-metal-oxide intercalation cathodes through the generation of localized electron holes on oxygen. *Nat. Chem.* **2016**, *8* (7), 684−91.
(37) Bunker, G. *Introduction to XAFS: A Practical Guide to X-Ray Absorption Fine Structure Spectroscopy*; Cambridge University Press: Cambridge, United Kingdom, 2010.
(38) Shirazi Moghadam, Y.; Dinda, S.; El Kharbachi, A.; Melinte, G.; Kübel, C.; Fichtner, M. Structural and Electrochemical Insights from the Fluorination of Disordered Mn-Based Rock Salt Cathode Materials. *Chem. Mater.* **2022**, *34* (5), 2268−2281.
(39) Bunker, G. B. *A X-Ray Absorption Study of Transition Metal Oxides*. Ph.D. Thesis, University of Washington, 1984.
(40) Ghigna, P.; Quartarone, E. Operando x-ray absorption spectroscopy on battery materials: a review of recent developments. *Journal of Physics-Energy* **2021**, *3* (3), 032006.
(41) Sottmann, J.; Bernal, F. L. M.; Yusenko, K. V.; Herrmann, M.; Emerich, H.; Wragg, D. S.; Margadonna, S. In operando Synchrotron XRD/XAS Investigation of Sodium Insertion into the Prussian Blue Analogue Cathode Material Na1.32Mn[Fe(CN)(6)](0.83)center dot z H2O. *Electrochim. Acta* **2016**, *200*, 305−313.
(42) Darwiche, A.; Murgia, F.; Fehse, M.; Mahmoud, A.; Iadecola, A.; Belin, S.; La Fontaine, C.; Briois, V.; Hermann, R. P.; Fraisse, B.; Berthelot, R.; Sougrati, M. T.; Monconduit, L.; Stievano, L. Operando X-ray absorption spectroscopy applied to battery materials at ICGM: The challenging case of BiSb's sodiation. *Energy Storage Materials* **2019**, *21*, 1−13.
(43) Fehse, M.; Iadecola, A.; Sougrati, M. T.; Conti, P.; Giorgetti, M.; Stievano, L. Applying chemometrics to study battery materials: Towards the comprehensive analysis of complex operando datasets. *Energy Storage Materials* **2019**, *18*, 328−337.
(44) Koga, H.; Croguennec, L.; Ménétrier, M.; Mannessiez, P.; Weill, F.; Delmas, C.; Belin, S. Operando X-ray Absorption Study of the Redox Processes Involved upon Cycling of the Li-Rich Layered Oxide Li1.20Mn0.54Co0.13Ni0.13O2 in Li Ion Batteries. *J. Phys. Chem. C* **2014**, *118* (11), 5700−5709.
(45) Li, B.; Sougrati, M. T.; Rousse, G.; Morozov, A. V.; Dedryvère, R.; Iadecola, A.; Senyshyn, A.; Zhang, L.; Abakumov, A. M.; Doublet, M.-L.; Tarascon, J.-M. Correlating ligand-to-metal charge transfer with voltage hysteresis in a Li-rich rock-salt compound exhibiting anionic redox. *Nat. Chem.* **2021**, *13* (11), 1070−1080.
(46) Källquist, I.; Naylor, A. J.; Baur, C.; Chable, J.; Kullgren, J.; Fichtner, M.; Edström, K.; Brandell, D.; Hahlin, M. Degradation Mechanisms in Li2VO2F Li-Rich Disordered Rock-Salt Cathodes. *Chem. Mater.* **2019**, *31* (16), 6084−6096.
(47) Yamada, A. Lattice Instability in Li(LixMn2-x)O4. *J. Solid State Chem.* **1996**, *122* (1), 160−165.
(48) Szymanski, N. J.; Lun, Z.; Liu, J.; Self, E. C.; Bartel, C. J.; Nanda, J.; Ouyang, B.; Ceder, G. Modeling Short-Range Order in Disordered Rocksalt Cathodes by Pair Distribution Function Analysis. *Chem. Mater.* **2023**, *35* (13), 4922−4934.